Electrical impedance controls mechanical sensing in ionic polymer metal composites

Youngsu Cha, Filippo Cellini, and Maurizio Porfiri*
Department of Mechanical and Aerospace Engineering, Polytechnic Institute of New York University, Brooklyn, New York 11201, USA
(Received 30 August 2013; published 23 December 2013)

Ionic polymer metal composites (IPMCs) are a class of soft electroactive materials that are recently finding extensive application as mechanical sensors and energy harvesters in liquids. In their most fundamental form, IPMCs are composed of a hydrated ionomeric membrane that is sandwiched between two electrochemically deposited metal electrodes. Ionomer swelling, counterion diffusion, and the formation of electric double layers are some of the physical phenomena underpinning energy transduction in IPMCs; however, a thorough understanding of the relative influence of such phenomena is yet to be established. Here, we propose a physics-based modeling framework, based on the Poisson-Nernst-Planck system, to describe IPMC chemoelectrical response to an imposed time-varying flexural deformation. We utilize the method of matched asymptotic expansions to compute a closed-form solution for the electric potential and counterion concentration in the IPMC. The model predicts that IPMC sensing is independent of the time rate of deformation and linearly correlated to the mechanical curvature, with a coefficient of proportionality that is a function of the ionomer thickness and the temperature. Thus, our results demonstrate that the characterization of IPMC electrical impedance suffices to identify all the parameters that are relevant to sensing, in contrast with the current state of knowledge. Theoretical results are validated through experiments on patterned in-house fabricated IPMC samples that are subject to time-varying flexural deformations.

DOI: 10.1103/PhysRevE.88.062603 PACS number(s): 61.41.+e, 82.45.Wx, 07.07.Df, 46.15.Ff

I. INTRODUCTION

Ionic polymer metal composites (IPMCs) are novel electroactive materials which are fabricated by sandwiching soft ionomeric membranes, such as Nafion [1–4] and Flemion [3,5], with noble metal electrodes, such as platinum [1,3,4] and gold [3,5]. IPMCs have received considerable attention in the past two decades for their propitious attributes as compliant actuators in liquids [1,6,7]. Specifically, they have been shown to produce large mechanical deformations in response to modest voltages applied across their electrodes and to react to time-varying voltage inputs of broad frequency contents [1,8,9]. These features have been especially beneficial in the design of miniature biomimetic propulsion systems [10–16] and micromanipulators [17–20]. The research impetus towards these engineering applications has been accompanied and supported by rigorous research on the physics of actuation [21–31]. As a result, our capacity to predict the performance of IPMC actuators as a function of physical and geometric parameters of their constituents is relatively well developed.

Recent efforts have demonstrated that IPMCs can accurately and precisely sense mechanical deformations in a broad range of operating conditions [32–40]. For example, IPMCs have been utilized in flow sensing [32], touch sensing [33], force sensing [34,35], and energy harvesting [36–40]. While recent modeling efforts [32,34,35,39,41–49] have helped us in identifying the determinants of IPMC sensing, our understanding of the physical phenomena that control energy transduction is still relatively limited, and the current practice in IPMC sensors' design cannot rely on predictive models.

In so-called black-box models, empirical rules are established on the basis of experimental observations on IPMC electrical response to mechanical deformations. For example, in Refs. [34,35,43], the short-circuit current of a cantilever IPMC is shown to linearly scale with the tip deflection and the associated transfer function is experimentally identified. For large quasistatic deformations, in Ref. [45], it is shown that the bending angle of a cantilever IPMC is linearly proportional to the peak open-circuit voltage and the coefficient of proportionality is experimentally identified. In Ref. [48], several lumped circuit sensor models comprising capacitors, resistors, and deformation-controlled current sources are presented and tested against experimental results.

A first comprehensive physics-based model of IPMC sensing has been proposed in Ref. [41]. The model revolves around the notion that the deformation of clusters in the ionomer core is central to sensing. As such, model calibration requires deep knowledge of the topology of the clusters along with a multitude of physical and geometric parameters, which hamper the direct application of the approach to design IPMC sensors and to dissect the relative role of the contributing factors. Building upon the work in Ref. [41], a series of more analytically tractable physics-based models based on different implementations of the Poisson-Nernst-Planck (PNP) system [50] have been proposed in Refs. [39,42,44,46,47,49,51]. While these models have helped in identifying the determinant processes underpinning IPMC sensing, that is, ionomer swelling, counterion diffusion, and the formation of electric double layers in the vicinity of the electrodes, their ability to predict IPMC sensing is rather limited. Indeed, most of these models require *a posteriori* use of *ad hoc* parameters to be identified from experimental data.

Common to all these models is the assumption that the IPMC core is a homogeneous material, which we argue is their main limitation. In fact, IPMCs are generally fabricated through an electroless chemical reduction process [2,52] consisting of the diffusion and adsorption of a noble metal salt in the polymer and its consecutive deposition on the ionomer

*mporfiri@nyu.edu; http://faculty.poly.edu/~mporfiri/index.htm

 ©2013 American Physical Society

surface through a reducing agent. Such deposition results in the formation of a metal particle layer, which is composed of scattered metal particles dispersed in the ionomer at the interface between the ionomer core and the metal electrodes; see, for example, microscopy results in [53,54].

In previous work of our group [55,56], we have introduced the notion of "composite layer" to describe IPMC electrical behavior in the vicinity of the electrodes. Therein, we describe the IPMC as a stacked sequence of five layers, where the polymer core is separated from the metal electrodes by two composite layers. This approach shares similarities with the theoretical concepts of inner electrode [57], intermediate layer [54], and active area [58,59]. We have already demonstrated that such composite layers can be integrated in PNP systems to explain the complex frequency dependence of IPMC impedance in Refs. [55,56]. Here, we extend this framework to study the chemoelectromechanical behavior of IPMCs in response to an imposed mechanical deformation. Specifically, we extend the formulation presented in Refs. [55,56] to account for the swelling of the ionomer core and the composite layers as well as the forced counterion convection associated with the IPMC motion. Following Refs. [60–63], we use the method of matched asymptotic expansions [64] to derive a closed-form solution for the electric potential and the counterion concentration in the IPMC, along with a distributed circuit model of IPMC sensing. The framework is validated through comparison with experimental data on IPMCs with varying number of plating layers, undergoing large periodic deformations at varying excitation frequency.

We organize the paper as follows. In Sec. II, we present the governing equations for the chemoelectromechanical response of IPMCs to mechanical deformations. In Sec. III, we establish closed-form solutions for the electrical potential and counterion concentration, along with a pertinent distributed circuit model. In Sec. IV, we validate the model through comparison with experimental results and discuss the main elements of our framework. Conclusions are summarized in Sec. V.

II. GOVERNING EQUATIONS

We model the IPMC chemoelectromechanical behavior by adapting the PNP framework originally developed in Refs. [27,65] to study IPMC charge dynamics and mechanical actuation. With reference to a two-dimensional scenario, IPMC chemoelectrical response is described in terms of the electrical potential ψ and the concentration of mobile counterions, with unit valency, per unit volume of deformed IPMC c. Both of these fields are functions of the time variable t and the two-dimensional coordinates in the deformed configuration x and y; see Fig. 1. For convenience, we set the voltage ground at the origin of the coordinate system $x = y = 0$. IPMC flexural deformations are modeled using the classical Euler-Bernoulli beam theory [66,67], whereby we assume that the IPMC kinematics is fully described by the rotation of the cross section φ, which depends only on t and y. Thus, IPMC cross sections are assumed to be rigid and to stay orthogonal to the midaxis, along y, during the deformation.

We further hypothesize that the IPMC is inextensible so that its length is always L and the rotation of the cross

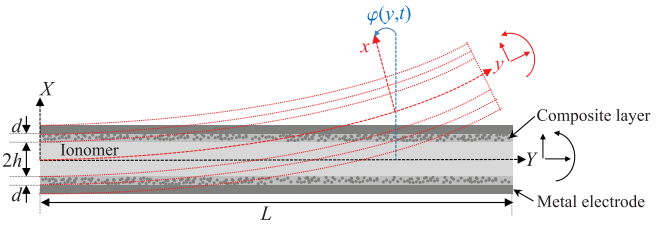

FIG. 1. (Color online) Schematics of the IPMC showing the clamping at $y = 0$ and the actions applied at $y = L$.

section φ is sufficient to describe the IPMC kinematics [67]. Indeed, assuming that the cross section at $y = 0$ is clamped as displayed in Fig. 1, the location of the IPMC midaxis is given by

$$\frac{\partial X_0(y,t)}{\partial y} = \sin(\varphi(y,t)), \tag{1a}$$

$$\frac{\partial Y_0(y,t)}{\partial y} = \cos(\varphi(y,t)), \tag{1b}$$

with $\varphi(0,t) = 0$ at every time. The position of any other point is computed from the location of the midaxis through

$$X(x,y,t) = X_0(y,t) + \cos(\varphi(y,t))x, \tag{2a}$$

$$Y(x,y,t) = Y_0(y,t) - \sin(\varphi(y,t))x. \tag{2b}$$

The dilatation in the IPMC is consistently computed from the deformation above as $\chi(x,y,t) = 1 - k(y,t)x$, where $k(y,t) = \frac{\partial\varphi(y,t)}{\partial y}$ is the IPMC curvature. With this notation, a positive curvature corresponds to a deformation similar to the one depicted in Fig. 1, that is, one in which the center of curvature resides in the region $x > 0$.

Following [55,56], we model the IPMC as the stacked sequence of five layers: an ionomer core, two composite layers of metal particle dispersed in the ionomer material, and two metal electrodes. For simplicity, each layer is assumed to have constant thickness and physical properties along the IPMC length and width. More specifically, each composite layer has thickness d, diffusivity D_{cl}, dielectric constant ϵ_{cl}, and polymer volume fraction ϕ. The ionomer has thickness $2h$, diffusivity D, and dielectric constant

$$\epsilon(x) = (\epsilon_{\mathrm{i}} - \epsilon_{\mathrm{b}})e^{-\mu\frac{h+x}{h}} + (\epsilon_{\mathrm{i}} - \epsilon_{\mathrm{b}})e^{-\mu\frac{h-x}{h}} + \epsilon_{\mathrm{b}}, \tag{3}$$

where ϵ_{i} and ϵ_{b} refer to the permittivity of the ionomer at the interface with the composite layers and in its bulk, respectively, and μ is the decay rate of the permittivity; see Refs. [30,56]. The through-the-thickness variation of the electric permittivity is used to account for the presence of the high surface rough electrodes [29,68,69]. Moreover, the concentration of fixed anions in the ionomer core in the undeformed configuration is c_0. The electrodes are considered as lossy planar conductors with surface resistivity ρ. Following Refs. [55,56], the composite layers are assumed to be much thinner than the ionomer, while having considerably higher permittivity and lower diffusivity, that is, $d \ll h$, $\epsilon_{\mathrm{cl}} \gg \epsilon_{\mathrm{i}}$, and $D_{\mathrm{cl}} \ll D$.

Observations in Refs. [49] suggest that nonlinear electromigration is a secondary phenomenon in IPMC sensing, which is well described by a linearized one-dimensional form of the PNP system, where the axial coordinate y is treated as a parameter. Within this framework, the PNP system reduces to a set of linear partial differential equations in x and t, which are coupled through their boundary conditions and are linearly forced by the IPMC curvature k. Below, we briefly present the system of equations and propose a closed-form solution based on the method of matched asymptotic expansions. Notably, the model differs from the state of knowledge in the field of IPMC sensing, whereby it includes, for the first time, the presence of composite layers, and it considers convective phenomena that are essential for accurately predicting IPMC response in a broad frequency range.

A. Ionomeric membrane

The linearized one-dimensional PNP system within the ionomer core is [49]

$$-\frac{\partial}{\partial x}\left(\epsilon(x)\frac{\partial\psi(x,y,t)}{\partial x}\right) = F\left[c(x,y,t) - c_0(1+xk(y,t))\right], \tag{4a}$$

$$\frac{\partial c(x,y,t)}{\partial t} - c_0 x\frac{\partial k(y,t)}{\partial t} = D\left[\frac{\partial^2 c(x,y,t)}{\partial x^2} + \frac{Fc_0}{\mathcal{R}T}\frac{\partial^2\psi(x,y,t)}{\partial x^2}\right], \tag{4b}$$

where $\mathcal{R}$ is the universal gas constant, T is the IPMC temperature, and F is the Faraday constant. Note that the right-hand side in the Poisson's equation (4a) represents the charge imbalance per unit volume of deformed ionomer, which depends on its dilatation. Such dilatation also determines the convective effect in the mass continuity equation (4b).

B. Composite layers

The PNP system for the composite layers is adapted from Eq. (4) by scaling the counterion concentration with respect to the polymer volume fraction and accounting for the different physical properties in these regions. By labeling relevant variables through the subscript "cl" and using the subscript $\pm$ to identify the field variables in the upper, $h < x < h+d$, and lower, $-(h+d) < x < -h$, composite layers, we find

$$-\epsilon_{\rm cl}\frac{\partial^2\psi_{\rm cl\pm}(x,y,t)}{\partial x^2} = F\left[c_{\rm cl\pm}(x,y,t) - c_0\phi(1+xk(y,t))\right], \tag{5a}$$

$$\frac{\partial c_{\rm cl\pm}(x,y,t)}{\partial t} - c_0\phi x\frac{\partial k(y,t)}{\partial t} = D_{\rm cl}\left[\frac{\partial^2 c_{\rm cl\pm}(x,y,t)}{\partial x^2} + \frac{Fc_0\phi}{\mathcal{R}T}\frac{\partial^2\psi_{\rm cl\pm}(x,y,t)}{\partial x^2}\right]. \tag{5b}$$

C. Boundary, interface, and initial conditions

The IPMC is assumed to be initially electroneutral, that is,

$$c(x,y,0) = c_0, \tag{6a}$$

$$c_{\rm cl\pm}(x,y,0)/\phi = c_0. \tag{6b}$$

Following Refs. [55,56], we hypothesize that the counterion concentration and the electric potential are continuous at the ionomer-composite layer interfaces, that is,

$$c(\pm h,y,t) = c_{\rm cl\pm}(\pm h,y,t)/\phi, \tag{7a}$$

$$\psi(\pm h,y,t) = \psi_{\rm cl\pm}(\pm h,y,t). \tag{7b}$$

We further assume that the ion flux and the electric displacements are continuous at the ionomer-composite layer interfaces, that is,

$$J(\pm h,y,t) = J_{\rm cl\pm}(\pm h,y,t), \tag{8a}$$

$$\mathcal{D}(\pm h,y,t) = \mathcal{D}_{\rm cl\pm}(\pm h,y,t). \tag{8b}$$

Here the ion fluxes are defined by

$$J(x,y,t) = -D\left[\frac{\partial c(x,y,t)}{\partial x} + \frac{Fc_0}{\mathcal{R}T}\frac{\partial\psi(x,y,t)}{\partial x}\right], \tag{9a}$$

$$J_{\rm cl\pm}(x,y,t) = -D_{\rm cl}\left[\frac{\partial c_{\rm cl\pm}(x,y,t)}{\partial x} + \frac{Fc_0\phi}{\mathcal{R}T}\frac{\partial\psi_{\rm cl\pm}(x,y,t)}{\partial x}\right]. \tag{9b}$$

Moreover, the electric displacements are defined by

$$\mathcal{D}(x,y,t) = -\epsilon(x)\frac{\partial\psi(x,y,t)}{\partial x}, \tag{10a}$$

$$\mathcal{D}_{\rm cl\pm}(x,y,t) = -\epsilon_{\rm cl}\frac{\partial\psi_{\rm cl\pm}(x,y,t)}{\partial x}. \tag{10b}$$

We note that continuity of the electric displacement and the ion flux automatically guarantees the continuity of the through-the-thickness current per unit surface $i(y,t)$, which is computed by evaluating $-[\frac{\partial\mathcal{D}(x,y,t)}{\partial t} + FJ(x,y,t)]$ at any x in the ionomer or $-[\frac{\partial\mathcal{D}_{\rm cl\pm}(x,y,t)}{\partial t} + FJ_{\rm cl\pm}(x,y,t)]$ at any x in the composite layers.

Following Ref. [62], we consider ion-blocking metal electrodes and, for convenience, we define the voltage difference between the electrodes as $v_{\rm s}$. Therefore, we set

$$J_{\rm cl\pm}(\pm(h+d),y,t) = 0, \tag{11a}$$

$$\psi_{\rm cl+}((h+d),y,t) - \psi_{\rm cl-}(-(h+d),y,t) = v_{\rm s}(y,t). \tag{11b}$$

We consider the case of lossy electrodes [44,70], for which Ohm's and Kirchhoff laws yield

$$\frac{\partial v_{\rm s}(y,t)}{\partial y} = -r_{\rm s}i_{\rm s}(y,t), \tag{12a}$$

$$\frac{\partial i_{\rm s}(y,t)}{\partial y} = i(y,t), \tag{12b}$$

where i_s is the current through the top or bottom electrode and r_s is the surface resistance of both the electrodes per unit IPMC length. The latter parameter is computed from the width b of the IPMC and the resistivity ρ as $r_s = \rho b$. We comment that during the deformation, the resistance per unit IPMC length of either electrodes may vary, yet their series connection is constant due to the underlying hypothesis of Euler-Bernoulli beam kinematics.

Finally, we always assume that the electrodes at $y = L$ are open circuited, so

$$i_s(L,t) = 0. \tag{13}$$

Thus, we treat the IPMC as a two-terminal network, for which we study the relationship between the input voltage $V(t) = v_s(0,t)$ and the current $I(t) = i_s(0,t)$.

III. CHEMOELECTROMECHANICAL RESPONSE

Due to the physical and geometrical symmetry of the problem with respect to the y axis and the structure of the governing equations comprising the linearized PNP system, see Eqs. (4)–(13), the chemoelectric response of the IPMC is skew symmetric with respect to the y axis. More specifically, in the polymer region

$$c(x,y,t) - c_0 = -c(-x,y,t) + c_0, \tag{14a}$$

$$\psi(x,y,t) = -\psi(-x,y,t), \tag{14b}$$

and in the composite layers

$$c_{cl+}(x,y,t) - c_0\phi = -c_{cl-}(-x,y,t) + c_0\phi, \tag{15a}$$

$$\psi_{cl+}(x,y,t) = -\psi_{cl-}(-x,y,t). \tag{15b}$$

We comment that such a skew-symmetric response is generally lost during actuation, due to nonlinear electromigration generated by the large voltage across the electrodes [28,29].

To derive a tractable closed-form solution of the overall PNP system in Eqs. (4)–(13), which represents a set of linear nonhomogeneous partial differential equations, we adapt the procedure presented in Ref. [56] for the analysis of IPMC nonlinear charge dynamics. Such a procedure is based on the method of matched asymptotic expansions with respect to the perturbation parameter $\delta = \frac{1}{Fh}\sqrt{\frac{\epsilon_i \mathcal{R}T}{c_0}} \ll 1$, which measures the ratio between the so-called Debye screening length $\lambda = \sqrt{\frac{\epsilon_i \mathcal{R}T}{F^2 c_0}}$, associated with the interfaces between the ionomer and the composite layers and the ionomer semithickness [62]. Following Ref. [56], we hypothesize that the physical and geometric properties of the IPMC are such that the aggregated nondimensional parameters $\epsilon^* = \frac{\epsilon_{cl}\delta}{\epsilon_i\phi}$, $D^* = \frac{D_{cl}}{D\delta}$, and $d^* = \frac{d}{h\sqrt{\delta}}$ are all on the order of 1 as δ approaches zero in the asymptotic analysis [64].

Differently than in Ref. [56], we account for the presence of a forcing term in the PNP system due to the imposed mechanical deformation and we neglect nonlinear electromigration and steric phenomena [28,71,72], which are unlikely to be relevant for sensing applications [49]. Therefore, for the sake of brevity, we present directly the results of the analysis and refer to Ref. [56] for an analogous derivation. We first offer the general solution of Eqs. (4)–(11), which depends on the unknown voltage drop across the electrodes v_s, and then we utilize Eqs. (12) and (13) to ultimately compute the sought chemoelectric fields and the overall IPMC response.

A. Counterion concentration and electric potential

In the ionomer core and in the composite layers, the unilateral Laplace transform of the concentration and the electrical potential are given by the following expressions:

$$\mathcal{L}[c](x,y,s) = c_0\left(\frac{1}{s} - A_1(y,s)e^{-\frac{(h-x)}{\lambda}} + A_1(y,s)e^{-\frac{(h+x)}{\lambda}} + x\mathcal{L}[k](y,s)\right), \tag{16a}$$

$$\mathcal{L}[\psi](x,y,s) = V_{th}\left(A_1(y,s)e^{-\frac{(h-x)}{\lambda}} - A_1(y,s)e^{-\frac{(h+x)}{\lambda}} + A_2(y,s)x\right), \tag{16b}$$

and

$$\mathcal{L}[c_{cl\pm}](x,y,s) = c_0\phi\left(\frac{1}{s} \mp A_1(y,s)e^{-\sqrt{\frac{s}{D_{cl}}}(x\mp h)} \pm x\mathcal{L}[k](y,s)\right), \tag{17a}$$

$$\mathcal{L}[\psi_{cl\pm}](x,y,s) = \pm V_{th}A_3(y,s)(h + d \mp x) \pm \frac{\mathcal{L}[v_s](y,s)}{2}, \tag{17b}$$

where $\mathcal{L}[\cdot]$ is the unilateral Laplace transform, s is the Laplace variable, and $V_{th} = \mathcal{R}T/F$ is the thermal voltage. The thermal voltage is controlled by the absolute temperature T, and at room temperature it is approximately equal to 26 mV. The function A_1 is given in terms of the voltage across the electrodes and the IPMC curvature by

$$A_1(y,s) = \frac{\frac{\mathcal{L}[v_s](y,s)}{2V_{th}} + h\mathcal{L}[k](y,s)}{1 + \frac{\phi h\sqrt{D_{cl}}\sqrt{s}}{D} + \frac{\lambda h}{D}s}. \tag{18}$$

The functions A_2 and A_3 are computed from A_1 and the curvature through

$$A_2(y,s) = \left(\frac{\phi\sqrt{D_{cl}}\sqrt{s}}{D} + \frac{\lambda}{D}s\right)A_1(y,s) - \mathcal{L}[k](y,s), \tag{19a}$$

$$A_3(y,s) = -\frac{\epsilon_i}{\epsilon_{cl}\lambda}\left(\frac{\phi}{\lambda}\sqrt{\frac{D_{cl}}{s}} + 1\right)A_1(y,s). \tag{19b}$$

Note that Eqs. (16) and (17) reduce to the solution presented in Ref. [56], when $\mathcal{L}[k](y,s) = 0$, upon neglecting nonlinearities and steric effects considered therein.

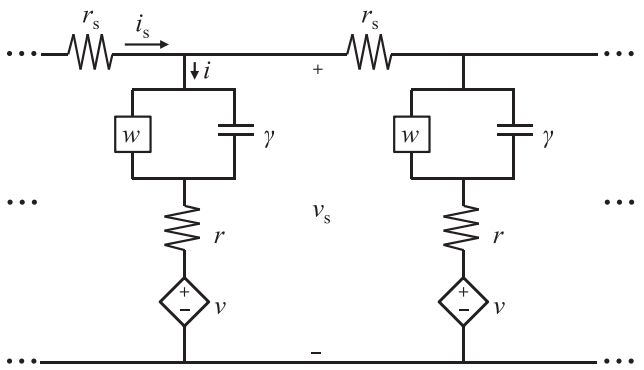

FIG. 2. Distributed circuit model of IPMC sensing.

B. Through-the-thickness current and voltage across the electrodes

From the concentration and the electric potential, we directly calculate the through-the-thickness current i in terms of the imposed curvature k and the voltage across the electrodes v_s. Specifically, in the Laplace domain, we find

$$\mathcal{L}[i](y,s) = \frac{1}{z(s)}(\mathcal{L}[v_s](y,s) - \mathcal{L}[v](y,s)), \tag{20}$$

where

$$v(y,t) = -2hV_{th}k(y,t), \tag{21}$$

with z is the through-the-thickness impedance per unit length (with units of $\Omega\,\mathrm{m}$). The impedance z is given by

$$z(s) = \frac{1 + (rw)\sqrt{s} + (r\gamma)s}{w\sqrt{s} + \gamma s}, \tag{22}$$

where $\gamma = \frac{\epsilon_i b}{2\lambda}$ is the capacitance per unit length associated with the double layers in the ionomer (with units of $\mathrm{F\,m^{-1}}$), $r = \frac{2h\lambda^2}{\epsilon_i D b}$ is the resistance per unit length associated with charge transport in the ionomer (with units of $\Omega\,\mathrm{m}$), and $w = \frac{\epsilon_i \phi b\sqrt{D_{cl}}}{2\lambda^2}$ is the Warburg impedance per unit length generated by charge diffusion in the composite layers (with units of $\mathrm{s^{1/2}\,\Omega^{-1}\,m^{-1}}$). By combining Eqs. (12) and (20), we obtain the equivalent circuit representation in Fig. 2, where the through-the-thickness impedance is synthesized as a simplified Randles' impedance [50] and the imposed deformation acts as a distributed voltage source in series connection.

We note that the proposed impedance model is similar to the black-box distributed model for actuation presented in Ref. [73]. On the other hand, it radically differs from the circuit models presented in Refs. [39,46,49] for the presence of a Warburg impedance in the through-the-thickness impedance and the distributed surface resistance. Both these elements are critical to accurately describe IPMC response. We also remark that the model in Ref. [39] posits that the deformation-controlled voltage source relates to the time rate of change of the curvature rather than the curvature as suggested in Eq. (21). Such discrepancy should be ascribed to the neglection of convective phenomena in Ref. [39], which are critical in shaping low-frequency IPMC sensing. Notably, a deformation-controlled voltage source is also predicted in Ref. [46]; however, the model presented therein is only applicable to static deformations and uses a peculiar dielectric polarization phenomena, instead of magnified dielectric constants to explain IPMC large capacitance, due the assumption of energy conservation.

Moreover, by Laplace transforming Eq. (12) and substituting Eq. (20), we find the general solution of the voltage across the electrodes and the surface current, namely

$$\begin{aligned}\mathcal{L}[v_s](y,s) = {} & B_1(s)e^{\sqrt{\frac{r_s}{z(s)}}y} + B_2(s)e^{-\sqrt{\frac{r_s}{z(s)}}y} \\ & - \frac{1}{2}\sqrt{\frac{r_s}{z(s)}}e^{\sqrt{\frac{r_s}{z(s)}}y}\int_0^y e^{-\sqrt{\frac{r_s}{z(s)}}y'}\mathcal{L}[v](y',s)dy' \\ & + \frac{1}{2}\sqrt{\frac{r_s}{z(s)}}e^{-\sqrt{\frac{r_s}{z(s)}}y}\int_0^y e^{\sqrt{\frac{r_s}{z(s)}}y'}\mathcal{L}[v](y',s)dy',\end{aligned} \tag{23a}$$

$$\begin{aligned}\mathcal{L}[i_s](y,s) = {} & -\sqrt{\frac{1}{z(s)r_s}}B_1(s)e^{\sqrt{\frac{r_s}{z(s)}}y} \\ & + \sqrt{\frac{1}{z(s)r_s}}B_2(s)e^{-\sqrt{\frac{r_s}{z(s)}}y} \\ & - \frac{1}{2z(s)}e^{\sqrt{\frac{r_s}{z(s)}}y}\int_0^y e^{-\sqrt{\frac{r_s}{z(s)}}y'}\mathcal{L}[v](y',s)dy' \\ & + \frac{1}{2z(s)}e^{-\sqrt{\frac{r_s}{z(s)}}y}\int_0^y e^{\sqrt{\frac{r_s}{z(s)}}y'}\mathcal{L}[v](y',s)dy',\end{aligned} \tag{23b}$$

where B_1 and B_2 are yet-to-be-determined functions of s.

C. Open-circuit voltage

For open-circuit conditions at the IPMC clamp, the current I is zero. On account of Eq. (13), B_1 and B_2 in Eq. (23) reduce to

$$\begin{aligned}B_1(s) = B_2(s) = {} & \sqrt{\frac{r_s}{z(s)}}\frac{\coth\left[\sqrt{\frac{r_s L^2}{z(s)}}\right] - 1}{4} \\ & \times \left(e^{2\sqrt{\frac{r_s L^2}{z(s)}}}\int_0^L e^{-\sqrt{\frac{r_s}{z(s)}}y'}\mathcal{L}[v](y',s)dy' \right. \\ & \left. + \int_0^L e^{\sqrt{\frac{r_s}{z(s)}}y'}\mathcal{L}[v](y',s)dy'\right).\end{aligned} \tag{24}$$

From Eqs. (23a) and (24), we find the Laplace transform of the open-circuit voltage $V_{oc}(t) = v_s(0,t)$,

$$\mathcal{L}[V_{oc}](s) = 2B_1(s). \tag{25}$$

For the special case of perfectly conducing electrodes, $r_s \to 0$,

$$B_1(s) = B_2(s) = -V_{th}h\frac{\mathcal{L}[\varphi](L,s)}{L}, \tag{26}$$

which yields $V_{oc}(t) = -2V_{th}h\varphi(L,t)/L$, in agreement with Ref. [49]. [Note that $\varphi(L,t)/L$ corresponds to the mean curvature of the IPMC $k_{mean}(t) = \frac{1}{L}\int_0^L k(y,t)dy$.] Thus, for highly conductive electrodes, the composite layers have a secondary role on the open circuit voltage, which is controlled by the ionomer swelling. In this case,

$A_1(y,s) = A_3(y,s) = 0$ and $A_2(y,s) = -\mathcal{L}[k](y,s)$, so the counterion concentration and the electric potential in the ionomer reduce to $c(x,y,t) = c_0(1 + xk(y,t))$ and $\psi(x,y,t) = -V_{\rm th}xk(y,t)$, respectively. In the composite layers, the concentration is $c_{\rm cl\pm}(x,y,t) = \phi c_0(1 \pm xk(y,t))$ and the potential is $\psi_{\rm cl\pm}(x,y,t) = \mp V_{\rm th}hk(y,t)$. For a positive curvature, as shown in Fig. 1, the counterion concentration per unit volume of deformed IPMC increases in the vicinity of the compressed electrode (top) and decreases close to the stretched one (bottom). This indicates that the net charge does not change and the IPMC is everywhere electroneutral during the deformation, with the counterion concentration balancing the variation of the fixed charge concentration per unit volume of deformed IPMC. The electric potential in the ionomer core decreases with x, so a larger voltage is generated on the bottom electrode. In this case, we find that no boundary layers develop at the interface.

D. Short-circuit current

For short-circuit conditions at the IPMC clamp, the voltage V is zero. On account of Eq. (13), B_1 and B_2 in Eq. (23) become

$$B_1(s) = -B_2(s) = \frac{1}{2}\sqrt{\frac{r_{\rm s}}{z(s)}}\frac{1}{1+e^{2\sqrt{\frac{r_{\rm s}L^2}{z(s)}}}} \times \left(e^{2\sqrt{\frac{r_{\rm s}L^2}{z(s)}}}\int_0^L e^{-\sqrt{\frac{r_{\rm s}}{z(s)}}y'}\mathcal{L}[v](y',s)dy' + \int_0^L e^{\sqrt{\frac{r_{\rm s}}{z(s)}}y'}\mathcal{L}[v](y',s)dy'\right). \quad (27)$$

From Eqs. (23b) and (27), we obtain the Laplace transform of the short-circuit current $I_{\rm sc}(t) = i_{\rm s}(0,t)$,

$$\mathcal{L}[I_{\rm sc}](s) = -\frac{2}{\sqrt{z(s)r_{\rm s}}}B_1(s). \quad (28)$$

Differently from the open-circuit voltage, even for highly conductive electrodes, the short-circuit current is highly influenced by the composite layers. Indeed, for $r_{\rm s} \to 0$, we have $\mathcal{L}[I_{\rm sc}](s) = 2hV_{\rm th}\mathcal{L}[\varphi](L,s)/z(s)$, showing the effect of the through-the-thickness impedance. Thus, the composite layers have a fundamental role in shaping the frequency content of the short-circuit current. In this case, a compact solution similar to the one presented for open-circuited electrodes for the time evolution of the concentration and electric potential cannot be found. With reference to the IPMC parameter values from Ref. [56] and reported in Table I for completeness, in Fig. 3, we display the through-the-thickness evolution of the counterion concentration and the electrical potential IPMC to a uniform step change in the curvature of $1/L$. Note that in this case the salient nondimensional parameters used for the perturbation analysis are as follows: $\delta = 5.80 \times 10^{-6}$, $d^* = 9.54$, $D^* = 11.92$, and $\epsilon^* = 1000$. Therein, we only report the time evolution of the counterion concentration and the electric potential for $x > 0$, due to symmetry.

Figure 3 demonstrates the presence of boundary layers in the concentration and potential profile, along with counterion diffusion in the composite layers, which are instead absent in the open-circuit response. Notably, while the IPMC is electroneutral in the ionomer bulk, the interface in the vicinity of the compressed electrode is negatively charged, due to the depletion of mobile counterions that cannot balance the negative charges of the backbone ionomer. We also comment that the results in Fig. 3 offer further verification that nonlinear electromigration is a secondary effect in IPMC sensing, whereby we find that the variation of the concentration with respect to the initial values are within 1% for a very significant deformation with curvature equal to $1/L$.

TABLE I. IPMC physical and geometric parameters from Ref. [56].

Parameter	Value
F (C mol^{-1})	96485
$\mathcal{R}$ (J mol^{-1} K^{-1})	8.314
T (K)	300
c_0 (mol m^{-3})	1200
h (μm)	100
d (μm)	2.3
ϕ	0.5
D (m^2 s^{-1})	1.19×10^{-10}
$D_{\rm cl}$ (m^2 s^{-1})	8.24×10^{-15}
$\epsilon_{\rm i}$ (F m^{-1})	1.51×10^{-9}
$\epsilon_{\rm b}$ (F m^{-1})	1.51×10^{-11}
$\epsilon_{\rm cl}$ (F m^{-1})	1.30×10^{-1}

Often IPMC sensors are utilized to study steady-state harmonic vibrations at a fixed frequency f [35,39,44,47]. In this case, IPMC curvature is of the form $k(y,t) = \mathrm{Im}[\hat{k}(y,f)e^{\mathrm{I}(2\pi f)t}]$, where I is the imaginary unit, Im[·] denotes the imaginary part, and $\hat{k}$ is the phasor of the curvature. The phasor of the steady-state short-circuit current $\hat{I}_{\rm sc}$ can be directly computed from Eq. (28) by replacing in the integrals

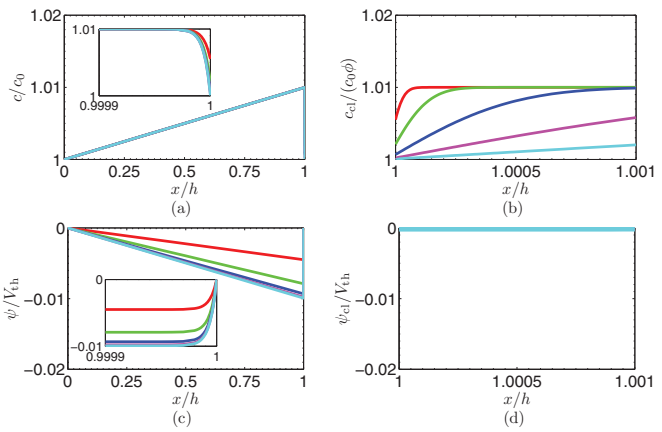

FIG. 3. (Color online) Theoretical predictions on the concentration of counterions and electric potential in an IPMC with perfectly conducting electrodes and properties in Table I in response to a uniform step in the curvature of $1/L$, for short-circuited electrodes. Red (gray), green (light gray), blue (darkest gray), purple (dark gray), and cyan (lightest gray) curves refer to $t = 0.001, 0.01, 0.1, 1$, and 10 s, respectively. (a) Counterion concentration in the ionomer; (b) counterion concentration in the composite layer; (c) electric potential in the ionomer; and (d) electric potential in the composite layer. Insets in (a) and (c) highlight the boundary layers at the interface between the ionomer an the composite layer.

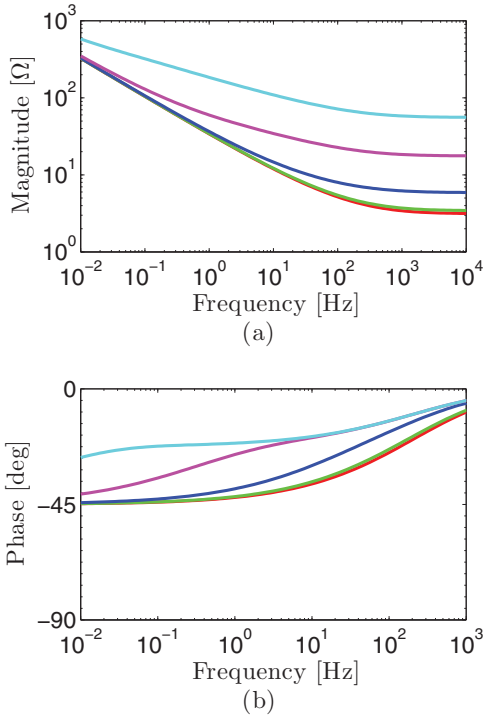

FIG. 4. (Color online) (a) Magnitude and (b) phase of the impedance of an IPMC with properties listed in Table I for different values of the surface resistance. Red (gray), green (light gray), blue (darkest gray), purple (dark gray), and cyan (lightest gray) represent $r_s = 10$, 100, 1000, 10 000, and 100 000 $\Omega\,\mathrm{m}^{-1}$, respectively.

of Eq. (27) $\mathcal{L}[k](y,s)$ with $\hat{k}(y,f)$ and setting $s = \mathrm{I}(2\pi f)$ in the impedance defined in Eq. (22). Here and henceforth, superimposed hat is used to identify phasors.

E. Overall impedance

From the open-circuit voltage V_{oc} and the short-circuit current I_{sc}, we compute the equivalent impedance of the IPMC, that is,

$$Z(s) = -\frac{\mathcal{L}[V_{oc}](s)}{\mathcal{L}[I_{sc}](s)} = \sqrt{z(s) r_s}\coth\left[L\sqrt{\frac{r_s}{z(s)}}\right]. \qquad (29)$$

With reference to the data in Table I, in Fig. 4, we display the IPMC impedance for $s = \mathrm{I}(2\pi f)$ and different values of the surface resistance. Figure 4 shows that increasing the surface resistance monotonically increases both the impedance magnitude and phase. In the high-frequency regime, where the IPMC is dominated by resistive effects, the equivalent resistance increases with $\sqrt{r_s}$. On the other hand, in the intermediate range around the knee of the magnitude curve, where reactive phenomena starts to be more evident, increasing the surface resistance regulates the slope of the impedance, which can attain values lower than -10 dB/decade with phases lower than -45°.

IV. EXPERIMENTS

We validate the proposed modeling framework through comparison with experiments on in-house fabricated IPMCs.

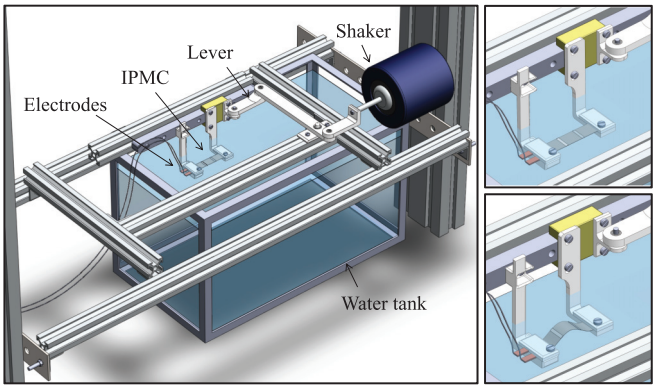

FIG. 5. (Color online) Computer-aided design of the experimental setup used for investigating IPMC sensing, illustrating the deformation of the IPMC strip in response to the linear motion of the movable clamp imposed by the shaker.

At room temperature, we conduct two integrated experiments to ascertain the effect of surface resistance on the IPMC impedance in Eq. (29) and verify the established relationship between the IPMC curvature and the short-circuit current in Eq. (28).

A. Experimental scheme

To produce a simple IPMC deformation similar to the one depicted in Fig. 1, we follow the methodology presented in Ref. [74], which offers a robust scheme to control IPMC curvature without the need of measuring forces. In this approach, IPMC strips are compressed along their axis through a movable fixture, whose relative motion with respect to a fixed clamp causes structural buckling. By electrically insulating the first portion of the strip in the vicinity of the fixed clamp, we produce an IPMC sample whose deformation is accurately regulated through the linear motion of a movable fixture.

Figure 5 displays a computer-aided design of the experimental apparatus, along with a detailed view of the buckling of the IPMC strip. A Bruel and Kjaer 4810 mini-shaker is controlled by an Agilent 33210A function generator to select the frequency of excitation and a Bruel and Kjaer 2718 power amplifier is used to adjust the amplitude of the motion. When the strip is undeformed, the distance between the clamps is 32 mm. We consider three nominal levels of IPMC deformation, by varying the peak-to-peak value of the sinusoidal motion of the movable clamp D_0 to include 2, 4, and 6 mm. For each value of D_0, we vary the input frequency from 2 to 5 Hz with an increment of 0.5 Hz, so each IPMC is tested in 21 conditions. The motion is analyzed through a IDT/Y3C high-speed camera, from which the trajectory of a marker on the movable clamp is measured through Motion studio [75] and Xcitex Proanalyst software [76]. The camera sampling rate is 250 frames per second to maintain a sampling frequency over 50 times the largest excitation frequency considered in this study of 5 Hz.

The electrodes of the strip are partitioned into three sections, following experimental observations in Ref. [74], and only the portion adjacent to the fixed clamp is used for sensing. Here and in what follows, we refer the portion of the strip

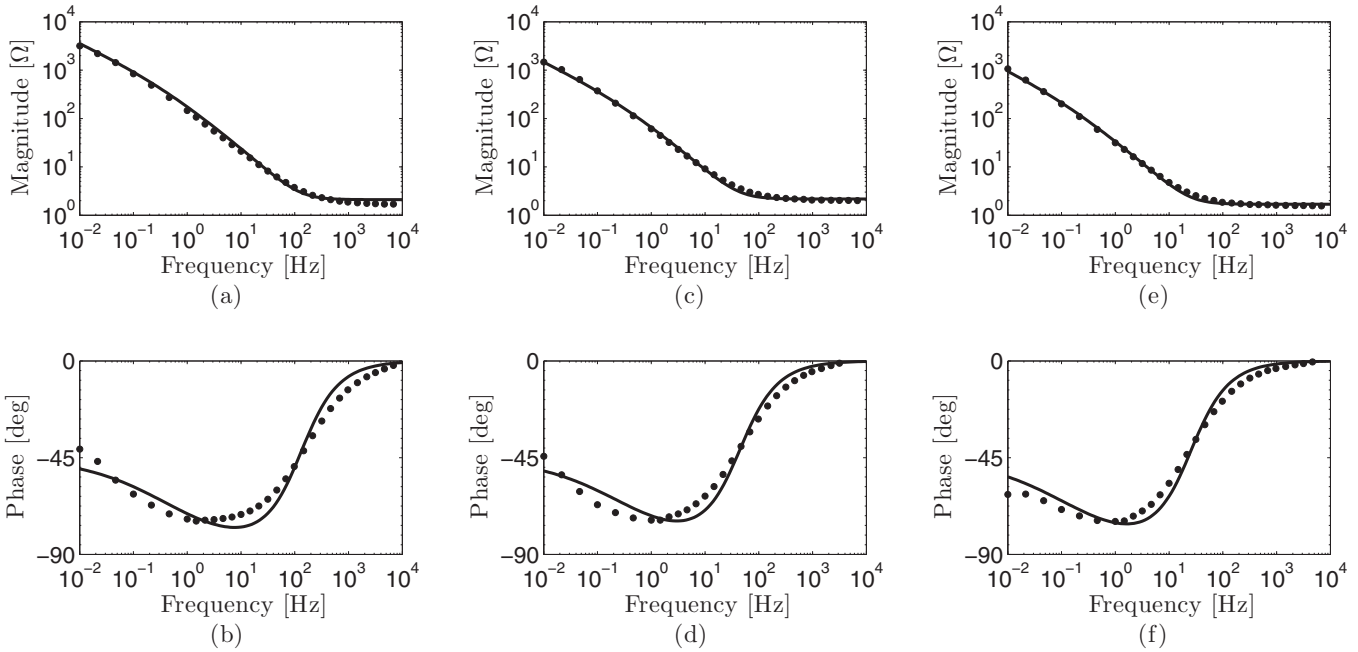

FIG. 6. Experimental data (dots) and theoretical prediction (solid lines) for the impedance of fully covered IPMCs. (a) Magnitude and (b) phase of the IPMC sample with one secondary plating cycle. (c) Magnitude and (d) phase of the IPMC sample with two secondary plating cycles. (e) Magnitude and (f) phase of the IPMC sample with three secondary plating cycles.

that is used for sensing as the IPMC sample or simply as the IPMC. The short-circuit current through the IPMC is measured through copper electrodes covering 3 mm of the sample and connected to an inverting amplifier, composed of a Texas Instruments TLC2202 low-noise precision operational amplifier with a feedback resistance of 10 kΩ. The output of the inverting amplifier is measured using a National Instruments data acquisition board 6221 and a custom-made code in Labview 8.6 with a low-pass filter at 60 Hz, a band-stop filter between 40 and 80 Hz, and another band-stop filter between 170 and 190 Hz, which are used to eliminate coupling with the power line. For each experiment, we acquire 3 s of data and we use a MATLAB script to process both the short-circuit current and the linear motion of the movable clamp to extract the amplitude of the phasors of both signals, with the frequency fixed to the input value.

Impedance measurements are performed using the methodology presented in Ref. [55], which is based on the "ac impedance" technique on a CH Instruments 700D potentiostat. Gold electrodes are used in the testing and the IPMCs are completely immersed in deionized water. The amplitude of the sine wave is set to 10 mV. To elucidate on the role of surface resistance, we systematically vary the portion of the samples which is covered by external electrodes. Specifically, we consider the following coverage values β: 100%, 75%, 50%, and 25%. A similar setup is utilized to measure the surface resistance, whereby gold electrodes are placed on the the top or bottom surfaces of the samples at a distance equal to 66% of their length. The resistance between the gold electrodes is estimated using a Fluke 175 true RMS digital multimeter. Also in these tests, the IPMCs are kept hydrated and the overall surface resistance r_s is evaluated by summing the surface resistance of the bottom and top electrodes.

B. IPMCs

IPMC strips are fabricated from Nafion N117 polymer membrane foils, produced by DuPont de Nemours, and platinum salt through an electroless chemical reduction process [2,52]. The IPMC strips have patterned electrodes, consisting of three identical portions on both the top and bottom surfaces. Patterning is obtained through a masking technique that uses 3M 5423 ultrahigh molecular weight polyethylene tape [4,77,78].

Briefly, the main fabrication steps can be described as follows. The masked Nafion membrane is immersed in a solution of $[Pt(NH_3)_4]Cl_2$ and NH_4OH overnight to allow platinum cations to diffuse through the ionomer. Following the adsorption phase, the sample is stored in deionized water, and a reducing agent $NaBH_4$ is added to reduce the platinum ions to metal particles on the ionomer surface. After this primary plating, IPMC strips are subject to repeated multiple secondary plating cycles to produce thicker electrodes. Specifically, more platinum is deposited by adding NH_2OH-HCl and NH_2NH_2 through a solution of $[Pt(NH_3)_4]Cl_2$, NH_4OH. After the deposition process is completed, the strips are neutralized in NaCl solution so Na^+ acts as the counterion species.

We fabricate three types of IPMC strips, which are characterized by one, two, or three cycles of secondary platinum plating. The nominal dimensions of each of them are 38 mm in length, 10 mm in width, and 0.2 mm in thickness. The gap between adjacent electrodes is 2 mm and the length of the three electrodes on each surface are 12, 10, and 12 mm, from one end to the other. This results into IPMC samples of length $L = 9$ mm when tested in the apparatus in Fig. 5, whereby 3 mm of the strip are covered by the copper electrodes, which activate only the first 12-mm-long portion of the strip.

TABLE II. Identified parameters of the IPMC samples.

Secondary plating	r (Ω m)	γ (F m^{-1})	w (s$^{1/2}$ Ω^{-1} m^{-1})	r_s (Ω m^{-1})
One cycle	0.0252	0.0485	0.0850	4450
Two cycles	0.0260	0.1397	0.2020	1875
Three cycles	0.0202	0.3113	0.2394	2862

C. Impedance measurements

Experimental data on fully covered IPMC samples are utilized to identify the parameters r, γ, and w defining the through-the-thickness impedance in Eq. (22) through least-squares error minimization [55]. Figure 6 displays experimental results against model predictions with identified parameters for the three IPMC samples. The model is able to accurately explain IPMC impedance in the whole frequency range. The minimal discrepancies in the phase for frequencies below 1 Hz should be attributed to experimental errors associated with the large impedance of the IPMCs. Results in Fig. 6 confirm that both the Warburg impedance and the IPMC capacitance are important parameters for describing IPMC electrical behavior in the range of frequencies typically considered for sensing, that is, 0.1–100 Hz [32,39,43]. Indeed, as the excitation frequency becomes smaller than 10 Hz, the effect of the Warburg impedance becomes stronger as seen in the bending of the impedance magnitude bending towards -10 dB/decade and the phase plot towards -45°.

The results of the identification are compactly presented in Table II. Our findings confirm the evidence presented in Ref. [55] on a larger batch of Nafion-based IPMCs. Specifically, we find that increasing the number of plating layers has a secondary role on the through-the-thickness resistance, which is controlled by the counterion diffusion in the ionomer bulk. On the other hand, increasing the number of plating layers is responsible for a significant increase of both the Warburg impedance and the double layer capacitance, which are controlled by interfacial properties. Table II also reports the measured values of the surface resistance of the electrodes. Such values are in agreement with experimental observations in Ref. [70], where surface resistance on the order of 1000 Ω m^{-1} are found. In contrast with our expectations, the surface resistance does not decrease with the number of plating layers, which is likely due to the formation of microcracks in the thicker electrodes [79].

The data in Table II are utilized to verify the effect of the surface resistance predicted by Eq. (29). Assuming that the IPMC does not deform during testing, the total impedance of a sample which is covered only for a fraction β of its length L can be computed as the parallel connection between the impedance of the free portion and the impedance of the electroded part. The former is calculated from Eq. (29) by substituting $(1-\beta)L$ with L, and the latter is simply $\frac{z}{\beta L}$. Thus, we find

$$Z_\beta(s) = \frac{\frac{z(s)}{\beta L}\sqrt{z(s)r_s}\coth\left[(1-\beta)L\sqrt{\frac{r_s}{z(s)}}\right]}{\frac{z(s)}{\beta L}+\sqrt{z(s)r_s}\coth\left[(1-\beta)L\sqrt{\frac{r_s}{z(s)}}\right]}. \tag{30}$$

Model predictions from Eq. (30) are presented in Fig. 7 for all the considered cases. The model is successful in accurately anticipating the effect of β on the impedance in Eq. (30), which regulates the magnitude of $Z_\beta(\mathrm{I}2\pi f)$ for f larger than 10 Hz and its phase for frequencies in the range 1–100 Hz. Specifically, decreasing the coverage of the sample is responsible for a remarkable increase in the high-frequency

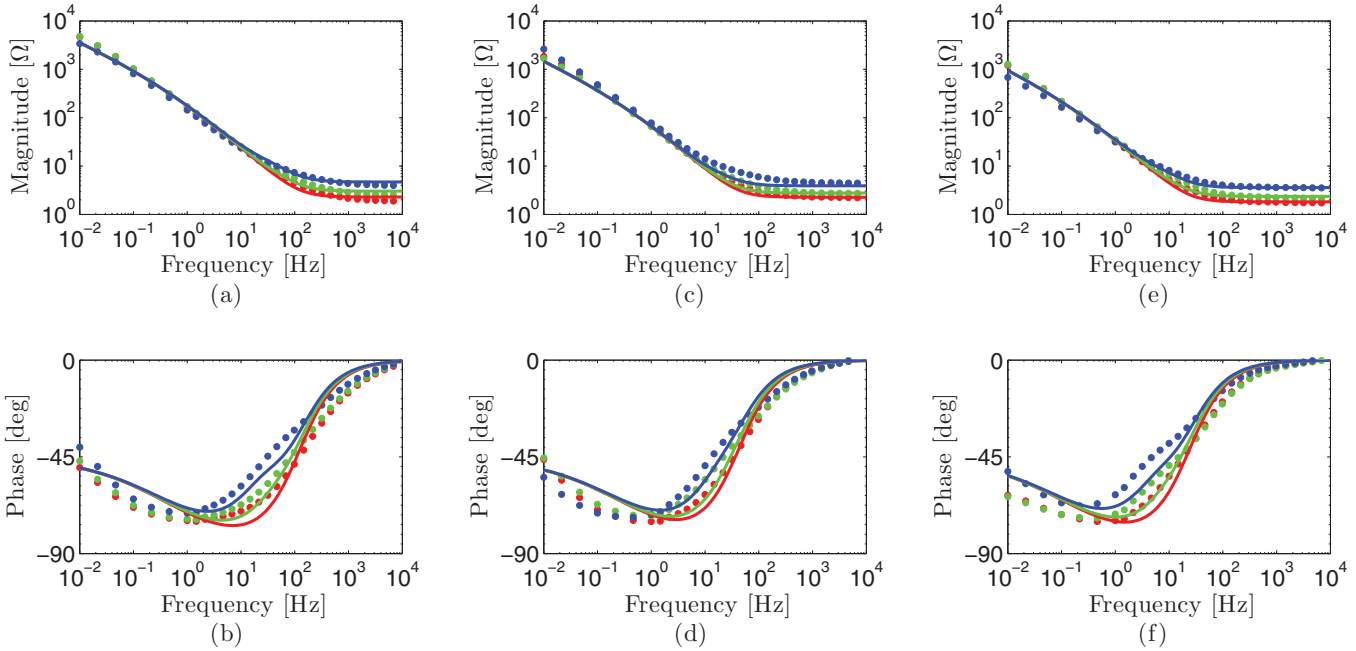

FIG. 7. (Color online) Experimental data (dots) and theoretical prediction (solid lines) for the impedance of partially covered IPMCs. (a) Magnitude and (b) phase of the IPMC sample with one secondary plating cycle. (c) Magnitude and (d) phase of the IPMC sample with two secondary plating cycles. (e) Magnitude and (f) phase of the IPMC sample with three secondary plating cycles. Red (gray), green (light gray), and blue (dark gray) refer to β equal to 75%, 50%, and 25%, respectively.

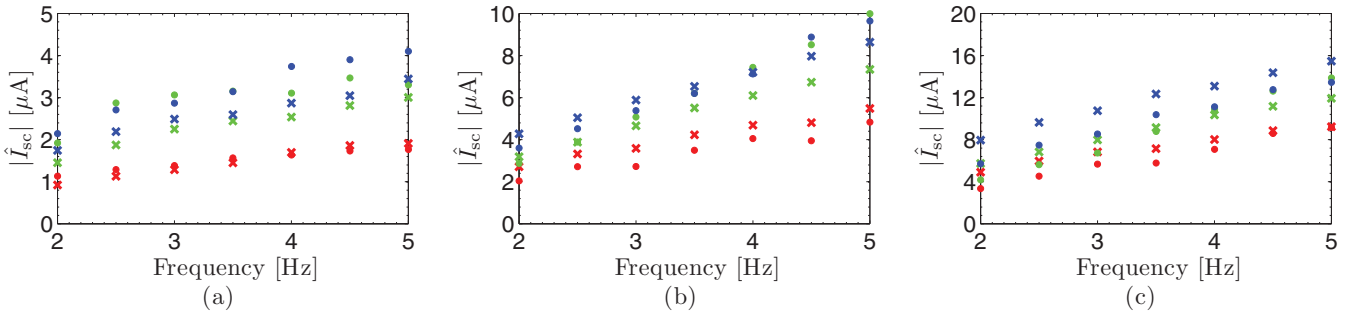

FIG. 8. (Color online) Amplitude of the short-circuit current through the IPMCs. (a) IPMC sample with one secondary plating cycle, (b) IPMC sample with two secondary plating cycles, and (c) IPMC sample with three secondary plating cycles. Red (gray), green (light gray), and blue (dark gray) refer to $D_0 = 2, 4, 6$ mm, respectively. Dots and crosses indicate experimental data and theoretical predictions, respectively.

magnitude of the impedance, which is related to resistive effects. At the same time, decreasing the coverage of the sample modulates the interplay between resistive and reactive phenomena that are visible in the variations of the phase in the frequency range 1–100 Hz.

D. Sensing

Following the approach presented in Ref. [74], and based on the closed-form results on beam post-buckling in Ref. [67], we compute the curvature along the whole IPMC strip from the sinusoidal motion of the movable clamp for each experimental condition. The curvature field is then sampled in the interval $[0, L]$, defining the IPMC sample, using 51 Gaussian quadrature points and the phasor at each location is extracted using a MATHEMATICA script. These data are ultimately used to perform the numerical integrations in Eq. (28) and compute the phasor of the short-circuit current stemming from the proposed modeling framework.

A comparison between model predictions and experimental results is presented in Fig. 8. Our findings are in good agreement with experimental results for all the 63 experiments conducted as part of this study, and the largest discrepancy between model predictions and experimental findings is on the order of 20%. The model is successful in predicting the dependence of the short-circuit current on the peak-to-peak oscillation and the excitation frequency of the movable clamp for different numbers of plating cycles. For each sample, we find that the short-circuit current increases as a function of the amplitude of excitation, which controls the curvature of the sample and, in turn, the voltage source v in Eq. (21); see Fig. 2.

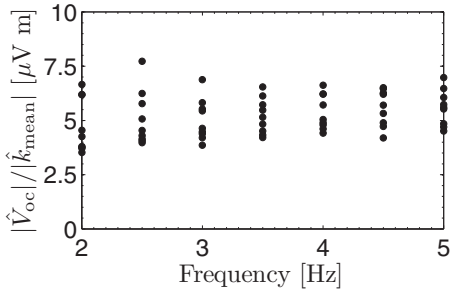

FIG. 9. Amplitude of the ratio between the phasor of the open-circuit voltage, extracted from experimental data, and the mean curvature as a function of the frequency of excitation.

Similarly, we find that the short-circuit current increases with the frequency of excitation, which is instead related to the reactive component of the IPMC impedance. Indeed, while the distributed voltage source depends on the curvature and not on its time rate of variation, see Eq. (21), the magnitude of the IPMC impedance decreases as a function of f, see, for example, Fig. 7. This causes the through-the-thickness current to increase. Finally, our results show that the number of plating cycles regulates the range of variation of the amplitude of the short-circuit current, whereby we find that for one plating layer the current can reach up to 4.096 μA while for three plating cycles we observe values as large as 13.857 μA. This should also be attributed to the increase in the reactive component of the impedance as a function of the number of plating cycles, see Table II, which results into a decrease in the through-the-thickness impedance.

These observations suggest that IPMC sensing can be enhanced by increasing the double layer capacitance and promoting counterion diffusion in the composite layers, which modulate the capacitance and the Warburg impedance of the IPMC. For example, for the sample with one secondary plating layer, if the capacitance were increased by a factor of 10, the amplitude of the phasor of the short-circuit current for $D_0 = 2$ mm and $f = 3.5$ Hz would increase from 1.449 to 7.537 μA. For the same condition, increasing the Warburg impedance of a factor of 10 would raise the current value to 3.868 μA.

The fact that the voltage source v is independent of the rate of change of the curvature can be further illustrated by computing the open-circuit voltage of the IPMCs from the short-circuit currents through the experimentally validated impedance model in Eq. (12). Specifically, we multiply the experimental data in Fig. 8 by the amplitude of the impedance in Eq. (12), computed at the pertinent input frequency, to estimate the amplitude of the phasor of the open-circuit voltage. To consolidate all these data points in a single graph, we divide each of these values by the corresponding amplitude of the mean curvature of the IPMC, computed from Gaussian quadrature. Such data are reported in Fig. 9, which confirms that the frequency has a secondary role on the open-circuit voltage. The average and standard deviation of these data

are 5.23 μV m and 0.98 μV m, respectively. Notably, for perfectly conducting electrodes, such data should collapse on a horizontal line at $2hV_{\text{th}} = 5\mu$V m. We comment that if a less accurate model of the impedance were utilized to extract open-circuit voltage data from measured short-circuit current, artificial dependencies on the curvature rate could arise, such as those often stemming from black-box models [40].

V. CONCLUSIONS

In this paper, we have presented a novel modeling framework to elucidate the physics of sensing in IPMCs. A PNP system is proposed to describe the evolution of the electric potential and counterion concentration in the IPMC in response to an imposed time-varying large deformation, which produces IPMC swelling and forced counterion convection. Composite layers have been utilized to model interfacial phenomena taking place in the vicinity of the electrodes, which have been treated as lossy conductors to model surface currents. A closed-form solution of the set of coupled partial differential equations has been computed using the method of matched asymptotic expansions. The solution has been leveraged to establish a mathematically tractable distributed circuit model of IPMC sensing, which is further specialized to relevant scenarios to offer physical insight into process of energy transduction. Model predictions have been validated through experiments on patterned IPMC strips undergoing large flexural deformations.

For highly conductive electrodes, we find that the IPMC is always electroneutral during the mechanical deformation if its electrodes are open circuited. Thus, the counterions do not migrate irrespective of IPMC swelling and a voltage drop develops across the electrodes to maintain electrochemical equilibrium. On the other hand, for short-circuited electrodes, boundary layers develop in the vicinity of the interfaces between the ionomer and the composite layers. In this case, the IPMC electroneutrality is lost in the boundary layers, where charge depletion and enrichment are elicited by the IPMC deformation, and in the composite layers, where counterion diffusion takes place. As the electrodes' resistance becomes significant, the voltage across the electrodes is not uniform along the IPMC span and significant variations of the overall impedance are observed across the entire frequency range. Specifically, surface resistance is demonstrated to differentially affect the high-frequency response of the IPMC, by increasing resistive effects, and the low-frequency response, by modulating double layer formation and counterion diffusion phenomena.

The model posits that IPMC sensing is controlled by electrical properties that can be identified *a priori* with traditional impedance analysis, and no additional *ad hoc* parameter is required for predicting the relation between the electrical output and the mechanical input deformation. Indeed, we find that the IPMC can be described through a distributed circuit model, where (i) the through-the-thickness charge dynamics is associated with a Randles impedance in series connection with a voltage source that is linearly proportional to the IPMC curvature and (ii) the surface charge dynamics is controlled by the surface resistance of the electrodes. The constant of proportionality between the voltage source and the curvature depends only on the ionomer thickness and the thermal voltage. In conclusion, this study shows that IPMC sensing is controlled by the electrical properties and accurate modeling of resistive and reactive phenomena suffices to establish predictive models of sensing.

ACKNOWLEDGMENTS

This material is based upon work supported by the National Science Foundation under Grant No. CMMI-0926791. The authors thank Mr. Hubert Kim for his valuable help in the experiments.

[1] M. Shahinpoor and K. J. Kim, Smart Mater. Struct. **10**, 819 (2001).
[2] K. J. Kim and M. Shahinpoor, Smart Mater. Struct. **12**, 65 (2003).
[3] S. Nemat-Nasser and Y. Wu, J. Appl. Phys. **93**, 5255 (2003).
[4] J. H. Jeon, S. W. Yeom, and I. K. Oh, Compos. Part A: Appl. Sci. Manufact. **39**, 588 (2008).
[5] K. Onishi, S. Sewa, K. Asaka, N. Fujiwara, and K. Oguro, Electrochim. Acta **46**, 737 (2001).
[6] R. Shankar, T. K. Ghosh, and R. J. Spontak, Soft Matter **3**, 1116 (2007).
[7] C. Jo, D. Pugal, I. K. Oh, K. J. Kim, and K. Asaka, Prog. Polym. Sci. **38**, 1037 (2013).
[8] K. Jung, J. Namb, and H. Choi, Sensors. Actuator. A **107**, 183 (2003).
[9] J. K. Park, P. J. Jones, C. Sahagun, K. A. Page, D. S. Hussey, D. L. Jacobson, S. E. Morgan, and R. B. Moore, Soft Matter **6**, 1444 (2010).
[10] M. Shahinpoor, Smart Mater. Struct. **1**, 91 (1992).
[11] B. Kim, D.-H. Kim, J. Jung, and J.-O. Park, Smart Mater. Struct. **14**, 1579 (2005).
[12] Z. Chen, S. Shatara, and X. Tan, IEEE/ASME Transact. Mechatron. **15**, 448 (2010).
[13] M. Aureli, V. Kopman, and M. Porfiri, IEEE/ASME Transact. Mechatron. **15**, 603 (2010).
[14] S. W. Yeom and I. K. Oh, Smart Mater. Struct. **18**, 085002 (2009).
[15] Z. Chen, T. I. Um, and H. Bart-Smith, Sensors Actuator. A **168**, 131 (2011).
[16] J. Najem, S. A. Sarles, B. Akle, and D. J. Leo, Smart Mater. Struct. **21**, 094026 (2012).
[17] S. Guo, T. Fukuda, K. Kosuge, F. Arai, K. Oguro, and M. Negoro, in *IEEE International Conference on Robotics and Automation*, Vol. 1 (IEEE, Nagoya, Japan, 1995), pp. 79–84.
[18] J. W. L. Zhou, H. Y. Chan, T. K. H. To, K. W. C. Lai, and W. J. Li, IEEE/ASME Transact. Mechatron. **9**, 334 (2004).
[19] M. Kruusmaa, A. Hunt, A. Punning, M. Anton, and A. Aabloo, in *IEEE International Conference on Robotics and Automation* (IEEE, Pasadena, CA, 2008), pp. 3588–3593.
[20] A. J. McDaid, K. C. Aw, E. Haemmerle, M. Shahinpoor, and S. Q. Xie, J. Micromech. Microeng. **21**, 125004 (2011).
[21] M. Shahinpoor, Smart Mater. Struct. **3**, 367 (1994).

[22] R. Kanno, S. Tadokoro, T. Takamori, M. Hattori, and K. Oguro, in *IEEE 21st International Conference on Industrial Electronics, Control, and Instrumentation* (IEEE, Orlando, FL, 1995), Vol. 2, pp. 913–918.

[23] P. G. de Gennes, K. Okumura, M. Shahinpoor, and K. J. Kim, Europhys. Lett. **50**, 513 (2000).

[24] K. Asaka and K. Oguro, J. Electroanal. Chem. **480**, 186 (2000).

[25] S. Nemat-Nasser, J. Appl. Phys. **92**, 2899 (2002).

[26] G. Del Bufalo, L. Placidi, and M. Porfiri, Smart Mater. Struct. **17**, 045010 (2008).

[27] T. Wallmersperger, B. J. Akle, D. J. Leo, and B. Kröplin, Compos. Sci. Technol. **68**, 1173 (2008).

[28] M. Porfiri, Phys. Rev. E **79**, 041503 (2009).

[29] B. J. Akle, W. Habchi, T. Wallmersperger, E. J. Akle, and D. J. Leo, J. Appl. Phys. **109**, 074509 (2011).

[30] P. Nardinocchi and M. Pezzulla, J. Appl. Phys. **113**, 224906 (2013).

[31] A. A. Lee, R. H. Colby, and A. A. Kornyshev, Soft Matter **9**, 3767 (2013).

[32] X. Chen, G. Zhu, X. Yang, D. L. S. Hung, and X. Tan, IEEE/ASME Transact. Mechatron. **18**, 932 (2013).

[33] I. S. R. Vedaraj, S. Parijaat, and B. V. A. Rao, Int. J. Adv. Manufact. Technol. **60**, 683 (2012).

[34] C. Bonomo, L. Fortuna, P. Giannone, S. Graziani, and S. Strazzeri, Smart Mater. Struct. **17**, 015014 (2008).

[35] P. Brunetto, L. Fortuna, P. Giannone, S. Graziani, and F. Pagano, IEEE Trans. Instrum. Meas. **59**, 1453 (2010).

[36] J. Brufau-Penella, M. Puig-Vidal, P. Giannone, S. Graziani, and S. Strazzeri, Smart Mater. Struct. **17**, 015009 (2008).

[37] R. Tiwari, K. J. Kim, and S. M. Kim, Smart Struct. Syst. **4**, 549 (2008).

[38] K. M. Farinholt, N. A. Pedrazas, D. M. Schluneker, D. W. Burt, and C. R. Farrar, J. Intell. Mater. Syst. Struct. **20**, 633 (2009).

[39] M. Aureli, C. Prince, M. Porfiri, and S. D. Peterson, Smart Mater. Struct. **19**, 015003 (2010).

[40] Y. Cha, M. Verotti, H. Walcott, S. D. Peterson, and M. Porfiri, Bioinspirat. Biomimet. **8**, 036003 (2013).

[41] S. Nemat-Nasser and J. Y. Li, J. Appl. Phys. **87**, 3321 (2000).

[42] K. Farinholt and D. J. Leo, Mech. Mater. **36**, 421 (2004).

[43] C. Bonomo, L. Fortuna, P. Giannone, S. Graziani, and S. Strazzeri, Smart Mater. Struct. **15**, 749 (2006).

[44] Z. Chen, X. Tan, A. Will, and C. Ziel, Smart Mater. Struct. **16**, 1477 (2007).

[45] E. Biddiss and T. Chau, Med. Eng. Phy. **28**, 568 (2006).

[46] M. Porfiri, Smart Mater. Struct. **18**, 015016 (2009).

[47] Y. Bahramzadeh and M. Shahinpoor, Smart Mater. Struct. **20**, 094011 (2011).

[48] K. Park and H. K. Lee, J. Korean Phys. Soc. **60**, 821 (2012).

[49] M. Aureli and M. Porfiri, Continuum Mech. Thermodyn. **25**, 273 (2013).

[50] A. J. Bard and L. R. Faulkner, *Electrochemical Methods: Fundamentals and Applications* (John Wiley & Sons, Inc., Hoboken, NJ, 2001).

[51] B. Akle and W. Habchi, in *Electroactive Polymer Actuators and Devices (EAPAD)*, Vol. 8687 (SPIE, San Diego, CA, 2013).

[52] M. Shahinpoor and M. Mojarrad, *Soft Actuators and Artificial Muscles* (US Patent 6.109.852, issued 29.08.2000.).

[53] X. L. Wang, I. K. Oh, J. Lu, J. Ju, and S. Lee, Mater. Lett. **61**, 5117 (2007).

[54] R. Tiwari and K. J. Kim, Appl. Phys. Lett. **97**, 244104 (2010).

[55] Y. Cha, M. Aureli, and M. Porfiri, J. Appl. Phys. **111**, 124901 (2012).

[56] Y. Cha and M. Porfiri, Phys. Rev. E **87**, 022403 (2013).

[57] S. J. Kim, S.-M. Kim, K. J. Kim, and Y. H. Kim, Smart Mater. Struct. **16**, 2286 (2007).

[58] B. J. Akle and D. J. Leo, Smart Mater. Struct. **16**, 1348 (2007).

[59] B. J. Akle and D. J. Leo, Smart Mater. Struct. **21**, 105034 (2012).

[60] M. Z. Bazant, K. T. Chu, and B. J. Bayly, SIAM J. Appl. Math. **65**, 1463 (2005).

[61] N. Abaid, R. S. Eisenberg, and W. Liu, SIAM J. Appl. Dynam. Syst. **7**, 1507 (2008).

[62] M. Porfiri, J. Appl. Phys. **104**, 104915 (2008).

[63] J. D. Davidson and N. C. Goulbourne, J. Appl. Phys. **109**, 084901 (2011).

[64] A. H. Nayfeh, *Perturbation Methods* (Wiley-VCH, Berlin, 2004).

[65] T. Wallmersperger, D. J. Leo, and C. S. Kothera, J. Appl. Phys. **101**, 024912 (2007).

[66] S. S. Antman, *Nonlinear Problems of Elasticity*, 2nd ed., edited by S. S. Antman, J. E. Marsden, and L. Sirovich, Applied Mathematical Sciences (Springer-Verlag, New York, 2004).

[67] A. Humer, Acta Mechanica **224**, 1493 (2013).

[68] B. J. Akle, T. Wallmersperger, E. Akle, and D. J. Leo, in *Proceedings of SPIE, Behavior and mechanics of multifunctional and composite materials*, edited by M. J. Dapino and Z. Ounaies (SPIE, San Diego, CA, 2008), Vol. 6929, p. 69290N.

[69] M. Aureli, W. Lin, and M. Porfiri, J. Appl. Phys. **105**, 104911 (2009).

[70] A. Punning, U. Johanson, M. Anton, A. Aabloo, and M. Kruusmaa, J. Intell. Mater. Syst. Struct. **20**, 1711 (2009).

[71] M. S. Kilic, M. Z. Bazant, and A. Ajdari, Phys. Rev. E **75**, 021502 (2007).

[72] M. S. Kilic, M. Z. Bazant, and A. Ajdari, Phys. Rev. E **75**, 021503 (2007).

[73] M. Shahinpoor and K. J. Kim, Smart Mater. Struct. **9**, 543 (2000).

[74] F. Cellini, Y. Cha, and M. Porfiri, J. Intell. Mater. Syst. Struct., doi:10.1177/1045389X13508333.

[75] http://www.idtvision.com/.

[76] http://www.xcitex.com/.

[77] K. J. Kim, D. Pugal, and K. K. Leang, Mar. Technol. Soc. J. **45**, 83 (2011).

[78] Y. Cha, L. Shen, and M. Porfiri, Smart Mater. Struct. **22**, 055027 (2013).

[79] K. Park, M. K. Yoon, S. Lee, J. Choi, and M. Thubrikar, Smart Mater. Struct. **19**, 075002 (2010).